

Combined Cantilever Beam and Optical Lever System for Mass Measurement of Individual Vials during Lyophilization

Elijah Bell^a, Xavier Bell^a, Umesh Padia^b, Sebastián Ruiz-Lopera^b, Liane Xu^{a,b}, Elena Kalodner-Martin^d (Comm. mentor), Rohan P. Kadambi^c (Mentor), Steven J. Burcat^a (Mentor) and Alexander H. Slocum^{a,*} (Mentor)

^aDepartment of Mechanical Engineering, Massachusetts Institute of Technology, 77 Massachusetts Ave, 02139, MA, USA

^bDepartment of Electrical Engineering and Computer Science, Massachusetts Institute of Technology, 77 Massachusetts Ave, 02139 Cambridge, USA

^dComparative Media Studies | Writing, Massachusetts Institute of Technology, 77 Massachusetts Ave, 02139 Cambridge, USA

^cDepartment of Chemical Engineering, Massachusetts Institute of Technology, 77 Massachusetts Ave, 02139 Cambridge, USA

ARTICLE INFO

Keywords:

Lyophilization
Water mass
Cantilever beam
Optical lever

ABSTRACT

Precise control of residual moisture is critical to drug stability and throughput in pharmaceutical lyophilization, yet current process-monitoring techniques provide only batch-averaged or post-process measurements of drying. We present a compact, individualized sensor that delivers in-line, milligram-level mass measurements throughout lyophilization without breaching sterility or requiring electrical connections within the chamber. Each vial is supported by a stainless steel cantilever, and mass loss during drying produces an angular deflection that is captured by a remote optical lever. A low-power laser diode reflects from a mirror bonded to the beam, and the resulting spot is amplified over a long optical path onto a high-resolution CMOS camera. A benchtop prototype was fabricated and calibrated over a 3 g range, and produced an RMSE of 0.62 mg. Repeated load/unload cycles demonstrated a repeatability of 9.2 mg. The cantilever remains in the elastic regime under full vial load, mitigating hysteresis, and the form factor allows 10 sensors to fit on a 180 mm × 120 mm magnetic levitation planar motor. The proposed sensor closes the metrology gap between primary and secondary drying, potentially enabling adaptive control strategies that shorten cycle times and ensure compliance with residual requirements for each vial individually. Ongoing work addresses optical-path folding, vibration damping, and material upgrades to deliver submilligram accuracy for a production-ready module in continuous lyophilization.

1. Introduction

Lyophilization, or vacuum freeze-drying, is a process that removes water from a solution by subjecting it to different temperatures and pressures. Vials with solution are first frozen, followed by a two-step drying process; during primary drying, the ice is sublimated by lowering the pressure, and during secondary drying, the remaining water is desorbed by applying heat [1]. After secondary drying, the residual water content left in the vial is typically 0.5 to 4 weight percent of the final dry product mass, on the order of 1 milligram [2].

Lyophilization is essential in pharmaceutical manufacturing for stabilizing pharmaceutical formulations, particularly biologics and vaccines. Removing water while maintaining product integrity extends the product's shelf life and lowers its storage condition requirements. Precise control of residual moisture is critical: insufficient removal can compromise product stability and efficacy [3, 4], while excessive drying can adversely affect reconstitution, protein denaturation, and overall lyophilization throughput [5]. These challenges directly impact patient safety, drug stability, and regulatory compliance, thus it is key to accurately ensure that moisture levels in final products are low across all vials in a batch.

To reach industrial throughput requirements, batches ranging from 1,000 to 100,000 individual vials are processed together in the same cycle. The whole process can take from hours to about one week due to the slow sublimation

*Corresponding author

✉ elibell@mit.edu (E. Bell); zoro@mit.edu (X. Bell); umesh@mit.edu (U. Padia); sruulo@mit.edu (S. Ruiz-Lopera); lianexu@mit.edu (L. Xu); Kalodner@mit.edu (E. Kalodner-Martin); kadambi@mit.edu (R.P. Kadambi); sburcat@mit.edu (S.J. Burcat); slocum@mit.edu (A.H. Slocum)
ORCID(s): 0000-0001-0000-0000 (E. Bell)

rates during primary drying [1]. Due to inherent heterogeneity during the process [6], the vials within the same batch may be in slightly different drying states at a given time, even if all initially contained the same solution. Therefore, the ability to monitor the mass of water in each vial individually can be crucial to ensuring that all vials are dry at the end while avoiding deliberate over-drying. Furthermore, time-resolved monitoring would allow for the optimization of cycle settings to ensure uniform drying at higher speeds leading to higher throughput.

Several techniques have been proposed and are currently used to assess moisture content during lyophilization. However, each one has its own significant limitations and there is yet no technique compatible with the lyophilization processes that provides the ability to measure water mass content of each vial in a batch individually inline. The pressure ratio and pressure rise tests provide estimates of water vapor flux within the lyophilizer [7, 8] providing continuous aggregate monitoring at the batch level. Advanced versions using tunable diode laser absorption spectroscopy have improved accuracy, but they still cannot detect vial-to-vial variations or identify individual vials that may fail to dry properly [9]. Karl Fischer titration and thermo-gravimetric analysis are the gold standards for measuring final residual moisture, but they require removing samples post-lyophilization, thus these processes unsuitable for inline monitoring [4]. Near-infrared spectroscopy (NIR) is a promising non-invasive solution, but it is constrained by sensitivity limitations and can only reliably measure a region of the product inside the vials, often that located near the chamber walls where drying conditions are different from the bulk of the batch [10, 11]. Recent work [12] has explored a spring-wire-based mass measurement system for individual vials during lyophilization. Although this system provides inline mass measurements of individual vials during lyophilization, the sensors suffer from calibration drift due to hysteresis effects introduced by mechanical movement, reducing absolute accuracy. As a result, the median reported precision was 50 mg, which may be sufficient to detect end-point for primary drying but is insufficient for secondary-drying which requires a higher resolution of approximately 1 mg.

This work proposes a sensing method to track the mass change in each individual vial of a batch during lyophilization. The method uses mechanical deflection that is directly related to changes in mass and is detected by a contactless optical sensor leveraging the optical lever principle. Concretely, a cantilever beam supporting each vial undergoes minute deflections as the vial loses mass and a laser reflected on the beam amplifies these small angular displacements by placing a viewing screen a distance away which is imaged by a camera to detect the laser spot displacement.

The optical lever technique is commonly used in precision metrology applications such as atomic force microscopy [13], where nanometer-scale displacements must be measured with high accuracy. By leveraging this principle, the proposed method for tracking individual mass change provides high sensitivity, inline, non-invasive measurements, robustness against mechanical drift, and compatibility with continuous lyophilization. A proof-of-concept system was prototyped and tested in a bench-top setup, achieving an accuracy of <3 mg (RMSE) over a 3 g range. Additional steps and considerations for future integration into a continuous lyophilizer for inline measurements are also discussed.

2. Materials and Methods

2.1. Functional Requirements

Resolution and Accuracy: Detecting mass changes at the milligram scale is critical because the residual moisture after secondary drying is on the order of 1 mg; any coarser resolution risks under- or over-drying, which can compromise product stability, denature proteins, and/or reduce lyophilization throughput.

Individualized Measurement: Because freezing and sublimation rates vary vial-to-vial, batch-level moisture measurements cannot detect under- or over-dried outliers. With individualized measurement, any vial exhibiting anomalous drying behavior can be flagged immediately for extended drying or removal.

Geometric Compatibility: Retrofitting an inline sensor into an existing maglev continuous lyophilizer demands that the sensor occupy no more space than is available on the 180 mm by 120 mm platform and achieve a packing density that maximally uses the chamber volume while maintaining airflow to the vials. Additionally, electrical wire passthroughs into the chamber should be avoided if possible, as that requires modification to the chamber's walls.

Environmental Compatibility: Lyophilization subjects materials to pressures as low as 30 Pa and temperatures down to -40°C during primary drying, then back to near-ambient conditions for secondary drying and unloading. The sensor must resist mechanical creep, optical drift, and calibration shifts across these extremes. All in-vacuum

components, including the cantilever array, mirrors, and mounting hardware, must be fabricated from vacuum-compatible alloys such as 17-4PH or 304 stainless steel and 6061 aluminum, which exhibit low outgassing and maintain high strength at cryogenic temperatures.

Non-destructiveness & Sterility: Pharmaceutical-grade lyophilization requires absolute sterility and avoidance of particulate generation. Sliding surfaces should be avoided inside the vacuum chamber, and external components must be sealed off, eliminating potential contamination pathways.

2.2. Strategy Exploration

Before selecting the combined cantilever beam and optical lever system, several strategies were initially investigated for water mass measurement. These included optical absorption, mechanical deflection (which encompassed the optical lever method), and capacitance sensing. Each strategy was further divided into multiple approaches. Through a process of down-selection based on feasibility assessments and the ability to meet performance requirements, only the most promising concept, the cantilever beam and optical lever system, was retained. A summary of the evaluated approaches is provided below.

2.2.1. Mechanical Deflection

The mechanical deflection strategy aimed to detect and measure changes in slope, resonance, or displacement of the tip of a cantilevered beam supporting a vial, resulting from variations in the mass of that vial. Tip displacement and resonance could often be measured by the same sensor, provided a sufficiently high sampling rate. The optical lever approach ultimately selected for this work falls within this category, alongside other designs that were investigated but rejected, such as traditional load cell stations and laser displacement sensors.

Load cell stations were investigated early in the design process for their ease of use. For instance, the Planar Motors system used in the continuous lyophilizer could be used to position a vial over a fork connected to the load cell before lowering the vial down onto it. Issues presented themselves when considering the requirement of the mechanical precision for said location, the time expense of picking-and-placing each vial on a weighing station, and the cost of a sufficiently precise load cell.

Laser displacement sensors were evaluated with the idea of measuring the displacement of the end of a cantilever beam that would hold the vial. This approach proved to be intractable, as a lever that would deflect sufficiently far under a 1 mg difference in load to be detectable by a laser displacement sensor would also be weak enough to yield and undergo plastic deformation.

The optical lever approach took inspiration from the laser displacement approach, but varied in the key difference that we would be measuring a change in angular deflection as opposed to change in distance. This approach would allow for signal amplification techniques to pick up on smaller changes in beam deflection.

2.2.2. Optical Absorption

The optical absorption strategy explored the use of near-infrared (NIR) spectroscopy to detect water's characteristic absorption peaks at 1400 nm and 1900 nm. However, the large diameter of the vials prevented sufficient transmission of light through the sample. Diffuse reflectance measurements were also attempted, but the heterogeneity of the lyophilized cakes led to inconsistent results. Additionally, efforts to detect water vapor in the headspace above the sample yielded no discernible signal change.

2.2.3. Capacitance-based moisture sensing

Because the relative permittivity of liquid water is extraordinarily high ($\epsilon_r \approx 78.4$) compared with that of a fully dried lyophilized product (e.g. sucrose $\epsilon_r \approx 3.3$) [14], monitoring capacitance during lyophilization could be used to infer residual moisture. We examined interdigitated coplanar electrode arrangements in which the electrodes reside directly beneath the vial (Figure 11). The 1% pharmaceutical residual moisture limit produces an estimated ΔC of 381 fF, comfortably within the resolution envelope of commodity capacitance meters.

Despite the favorable signal, several practical issues outweighed the theoretical advantages. The relative permittivity of a lyophilized matrix is formulation-dependent, requiring a calibration for each drug or excipient. The scheme also demands electrical feed-throughs into the vacuum chamber and precise vial seating to maintain measurement reproducibility. For these reasons, we ultimately pursued alternative measurement strategies. Further discussion of the capacitance strategy can be found in Appendix C.

2.3. Selected Strategy Overview

Our design utilizes per-vial cantilever beams, each functioning as both an individual support structure and an integrated mass sensor, in conjunction with a contactless optical-lever readout system, as illustrated in Figure 1. Each vial rests on a sterile, autoclavable beam tip that begins the lyophilization process in a maximally deflected state. As water mass is removed during drying, the beam unloads, resulting in a change in its angular orientation and vertical displacement. A small mirror, bonded to the free end of each cantilever beam, reflects a low-power diode laser toward a screen located at a long optical path length. This arrangement converts the beam's angular deflection into a lateral displacement of the laser spot on the screen. The mechanical principles governing this behavior are detailed in Appendix Governing Physics.

The laser spot is imaged using a high-resolution camera, enabling microradian-scale detection of angular deflections α induced by milligram changes in mass. The system's optical amplification increases with the length of the optical path (from the mirror to the screen). To avoid contamination and maintain vacuum integrity, both the laser and camera are located outside the lyophilization chamber, behind a vacuum-sealed, anti-reflection-coated window. This configuration eliminates the need for electrical passthroughs into the chamber. Because all optical components are located outside the lyophilizer, the original vial layout, chamber dimensions, and electrical passthroughs remain unchanged. For sequential data acquisition, a magnetic levitation (maglev) motion stage (Planar Motors) repositions each vial beneath the optical window. To maximize packing density, we use the shortest possible beam length that still achieves a mass resolution of 1 mg while staying within the beam's elastic deformation range, and we laterally offset the cantilevers to fit 10 vials in an interdigitate design within the 180 mm \times 120 mm footprint of the platform.

2.4. Mechanical Design

A schematic of the beam design is shown in Figure 2 alongside the fabricated prototype. The cantilever beams are fabricated from 304 stainless steel, an alloy chosen because it maintains its mechanical properties through the lyophilization cycle. To ensure a 1 mg change in mass would correspond to a measurable laser spot shift by the detector camera, the geometry of the beam was optimized through analytical modeling (Appendix Governing Physics). The beams have a thickness $t = 0.2$ mm, width $w = 10$ mm, and total length $L = 53$ mm selected to balance deflection sensitivity with mechanical robustness under the gravity load of the vial that is placed at $l = 35$ mm from the fixed end. Each cantilever features an integrated mirror (43-866, Edmund Optics) bonded to the beam, allowing for reflection of the laser beam with minimal added mass. The vial is held in place with three kinematic couplings cut with the beam itself and bent upwards. To avoid particulate generation and ensure sterilization compatibility, all bonds can be made using vacuum-rated, low-outgassing adhesives that withstand autoclave cycles and cryogenic conditions.

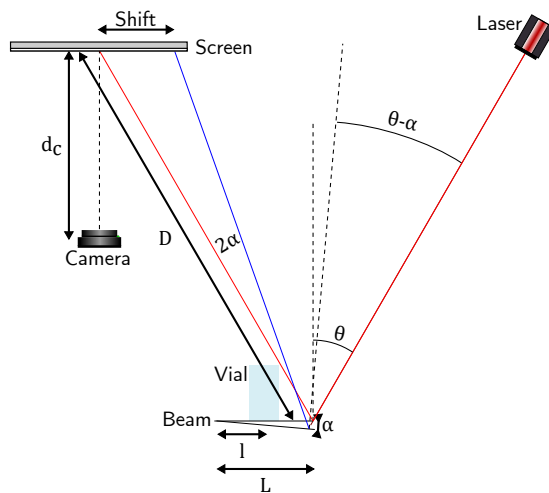


Figure 1: General schematic of the proposed strategy for mass measurement combining mechanical deflection and optical lever detection. The vial rests on top of a cantilever beam with its center at a distance l from the fixed-end. A laser reflected at the tip of the beam hits a screen at a far distance $D \gg l$ and the spot is imaged with a camera located at a distance d_c from the screen. Minute beam deflections α are amplified as large shifts at the screen.

Cyanoacrylate glue is easily attainable and suffices for this purpose. External to the lyophilizer, the optical detection system includes a red laser and a camera (B0483, Arducam) based on a high-resolution CMOS sensor (OV64A40, Omnivision) positioned at a distance d_c from a viewing screen that is located at a distance D from the mirror. The distance D can be tuned to provide the desired optical lever amplification based on Eq. (1) derived in the mathematical model in Appendix Governing Physics,

$$D = \frac{4\delta_{\text{res}} E^2 I^2}{m_C l^2 W \cos \theta (lhW + EI)}. \quad (1)$$

We formulated this model by combining the cantilever beam deflection with the optical lever principle, assuming the center of mass of the vial is offsetted vertically to account for the effect of tilting. In Eq. (1), δ_{res} is the minimum detectable laser-spot shift (determined by the camera characteristics and the detection algorithm), E is the Young's modulus of the beam material (193 GPa for 304 stainless steel), $I = \frac{wt^3}{12}$ is the second-moment of inertia of the beam's rectangular profile, l and h are respectively the horizontal and vertical distance between the fixed end of the beam and the center of mass of the vial when there is no deflection, $W = 9.81 \mu\text{N}$ is the target minimum detectable weight change, θ is the incidence angle of the laser with respect to the beam's normal when there is no deflection, and $m_C = -0.05$ is the camera magnification for a focal length of 6.65 mm and working distance of $d_c = 140$ mm.

It is important to ensure that the cantilever beam remains within the elastic region by not exceeding the material's yield strength. Although the sensing mass range is about 3 g, the entire weight of the vial with cap add an extra mass of about 15 g. The maximum stress on the beam with the selected geometry was calculated to be 110 MPa which is below half of the yield strength of 304 stainless steel (215 MPa), for a mass of 25 g well above the expected mass. This ensures that during normal operation the beam stays within strictly elastic deformation, thereby preventing hysteresis.

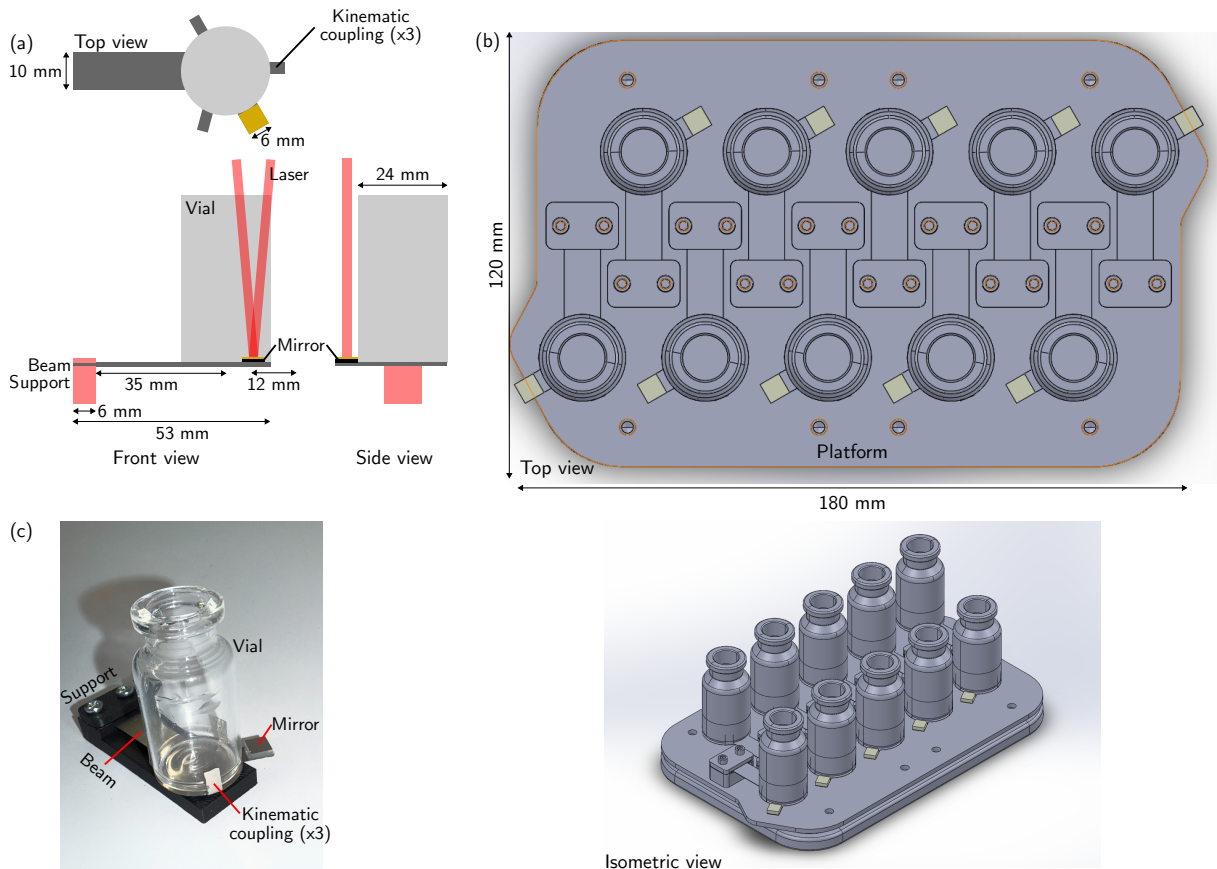


Figure 2: (a) Design of a individual mass sensing system and (b) proposed arrangement in a maglev platform. (c) Picture of the fabricated prototype cantilever beam sensor.

2.5. Sensing

The sensing system leverages an optical lever configuration to amplify minute angular deflections of the cantilever beams into detectable displacements on a CMOS camera sensor. The laser is aligned to the cantilever mirror by positioning the maglev platform so that the desired sensor is directly underneath the optical window. We chose a low power laser diode (<5mW) to minimize thermal loading while maintaining sufficient signal-to-noise ratio at the camera. For a given measurement, the CMOS camera takes N images $S^{(i)}[p, q]$ of the screen illuminated by the laser from which the centroid position $\mathbf{c}^{(i)} = (x_c^{(i)}, y_c^{(i)})$ is calculated as

$$x_c^{(i)} = \frac{\sum_{p=1}^P \sum_{q=1}^Q p \tilde{S}^{(i)}[p, q]}{\sum_{p=1}^P \sum_{q=1}^Q \tilde{S}^{(i)}[p, q]}, \quad y_c^{(i)} = \frac{\sum_{p=1}^P \sum_{q=1}^Q q \tilde{S}^{(i)}[p, q]}{\sum_{p=1}^P \sum_{q=1}^Q \tilde{S}^{(i)}[p, q]} \quad (2)$$

where $\tilde{S}^{(i)}[p, q] = S^{(i)}[p, q] - S_b[p, q]$ is the background-subtracted image of size $P \times Q$ with p and q representing pixel indexes. The background image $S_b[p, q]$ is taken with the laser off, ideally for every mass measurement since the maglev motion may change the background configuration. The estimated centroid for the mass measurement is the average of the individual centroids $\mathbf{c} = (\sum_i x_c^{(i)}, \sum_i y_c^{(i)})$, which improves centroid detection accuracy. The laser shift $s = \|\mathbf{c} - \mathbf{c}_0\|_{p_s}$ can be computed as the Euclidean distance $\|\cdot\|$ from the current centroid position to a reference centroid position \mathbf{c}_0 , scaled by the pixel size $p_s = 1.008 \mu\text{m}$. The reference centroid can be obtained from a second laser reflected on a different mirror located at a reference location such as at the fixed-end of the beam or close to it, which would make the system robust to re-positioning errors of the maglev platforms. For a static setup, \mathbf{c}_0 can be set as the centroid of the first measurement, reducing system complexity. In practice, the sensor can be aligned such that the laser spot moves along a single axis and one single centroid position can be analyzed. The measured centroid s can be mapped into mass m by using

$$m = \frac{EI}{2glh} \left(\sqrt{1 + \frac{16h}{lDm_C \cos \theta} s} - 1 \right), \quad (3)$$

where g is acceleration due to gravity. Note that for $h \rightarrow 0$,

$$m = \frac{4EI}{gl^2 Dm_C \cos \theta} s, \quad (4)$$

following a linear relationship as expected when the center of mass of the vial is aligned with the cantilever beam, however the general case of Eq. (3) is not linear. Linearization can be achieved by adding weight to the vial at the bottom to bring the center of mass down, while making sure the added mass is such that the yield strength of the material is still not exceeded.

To determine the precision of the centroid detection, 1000 centroid measurements were recorded in a static configuration with an empty vial using the prototype described in Section Testing Procedure. The average mean standard deviation of the measured centroids were $0.26 \mu\text{m}$ and $0.25 \mu\text{m}$ for the x and y axes respectively. Setting $\delta_{\text{res}} = 0.26 \mu\text{m}$ in Eq.(1) yields $D = 3.1 \text{ m}$, the theoretical minimum optical lever distance to be able to detect 1 mg mass changes. During operation, the beam oscillation may affect the centroid detection affecting the mass estimation.

The sensors arrangement shown in Fig. 2(b) would allow to use a single probe laser, two reference lasers and a single camera to probe all 10 vials in a single maglev platform one a time, using the entire field of view of the camera ($185 \text{ mm} \times 140 \text{ mm}$ at 140 mm working distance).

Simultaneous measurement may also be possible with the camera wide field-of-view of $185 \text{ mm} \times 140 \text{ mm}$ at a working distance of 140 mm , if probe and reference lasers are placed for each sensor position. Further considerations must be made such as optimizing the camera position to avoid clipping any laser path, suitable algorithms to detect all laser spots simultaneously in a single image, while being robust to cross-talk between laser spots.

3. Testing Procedure

The developed bench-top mass sensing and calibration system consisted of four components as shown in Figure 3: the cantilever beam, the optical probing system (laser and camera pair), an analytical balance for ground-truth mass measurement and a programmable syringe pump.

Two prototype cantilever beams were made. Prototype I with $l = 30$ mm was used to test different optical lever distances. Prototype II with $l = 35$ mm was designed after, with optimal dimensions for the maglev platform and was used for repeatability tests. The cantilever beams were water-jet cut from a 0.2 mm 304 stainless steel shim and attached to a 3D printed support via friction between two holders.

The red laser and the camera were mounted on an aluminum frame. The laser provided yaw and pitch adjusters that were used to steer the laser onto the mirror on the cantilever beam below it.

Four configurations (C1–C4) were tested using prototype I with different laser path lengths D . In C1, the camera imaged a laser spot reflected vertically to a screen $D \approx 0.6$ m above the cantilever. In C2, a steering mirror redirected the beam downward to a screen $D \approx 1.3$ m away. In C3, the laser was redirected horizontally to a screen at $D \approx 14.3$ m, while in C4 the same distance was used but we manually dosed water using a 20 μL pipette to produce more reliable ground-truth mass values. Detailed calculations of the expected accuracy for each configuration, and the calibration procedure using the analytical balance, are provided in Appendix A.1 and Appendix A.2.

To obtain a calibration curve of laser spot centroid shift versus mass and quantify the system accuracy, the syringe pump was controlled together with laser centroid detection using the camera and mass measurement using the analytical balance with accuracy of 0.1 mg. The calibration routine sequentially dosed a mass δm into the vial, followed by a 5 s pause to wait for the oscillations of beam due to the water dosing to settle down, and followed by recording $N = 10$ pairs of centroid position and mass ($\mathbf{c}^{(i)}, m^{(i)}$). To cover a mass range of Δm , the procedure was repeated $\left\lceil \frac{\Delta m}{\delta m} \right\rceil$ times.

Water evaporation during the recordings were deemed negligible owing to the relatively fast recording time per data point (≈ 10 s). A second-order polynomial was fitted to the averaged data points (\mathbf{c}, m) and the mass accuracy was determined as the root mean squared error (RMSE) of the fit.

A repeatability test was done with prototype II by generating five calibration curves in configuration C1. In each iteration, the vial was taken out the beam to empty it and then put back, simulating actual usage cycles. Leave-one-out cross-validation was performed by linearly fitting the data from four datasets and testing the linear fit with the remaining dataset, resulting in 5 possible combinations.

4. Results and Discussion

Calibration curves were obtained for all four testing configurations and are shown in Figure 4. For each data point, the 10 pairs of centroid position and mass measurements are plotted on top of the second-order linear fit. As expected, increasing the distance D increases the gain of the optical lever, effectively improving the sensitivity to mass changes; a smaller mass change produces a larger laser spot shift. This can be observed in the slope of the curves, which represents change in mass per millimeter change in centroid position, in Fig. 4. They go from steep for C1 to relatively flat for C3 and C4. Table 1 summarizes the calibration parameters and results for the three configurations. The experimental RMSE values are close to the lower bound resolution and show a decreasing trend as D increases, improving the mass accuracy as measured by the RMSE from 5.50 mg for C1 to 1.12 mg for C3. Despite the very long distance, C3 did not provide sub-mg accuracy. This was an unexpected result because theoretically as calculated in section B.2, accuracy should increase approximately linearly with laser path length. The discrepancy can be attributed to the imprecise ground-truth mass measurements which we characterized to have a ~ 0.8 mg standard deviation from 1000 continuous measurements in a static setup of a constant mass on the balance. Since the balance readings were not stable, the calibration was referencing an inaccurate ground-truth. Configuration C4, which uses pipetting as ground-truth reference instead of the balance, provided a sub-mg accuracy, the expected result given the laser path distance.

The dataset of configuration C1 was digitally downsampled to produce two calibrations curves, one with the entire target mass range 3 g and one with half range 1.5 g to match C2. The full-range calibration $\Delta m = 3$ g with a fine step $\delta m = 30$ mg demonstrates the ability to detect mass changes during the whole lyophilization process as shown in Figure 5. Importantly, the RMSE of 5.81 mg for the full-range calibration is not significantly larger than the one for the calibration with half the mass range (5.50 mg RMSE), meaning calibrating with using a shorter mass range, which

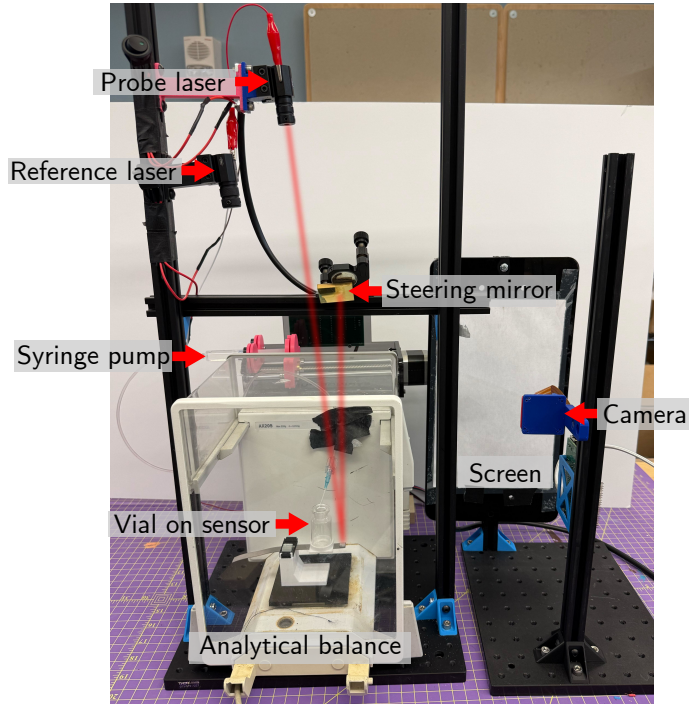


Figure 3: Prototype to evaluate and calibrate the mass sensing system, in configuration C3 (i.e., with the camera and screen separated from the main frame, and the steering mirror at 45 deg).

Configuration	Distance D (m)	Δm (g)	$\delta m(mg)$	Lower bound resolution (mg)	RMSE (mg)
C1	0.6	3	30	5.1	5.81
C2	1.3	1.5	100	2.4	3.02
C3	14.3	0.2	30	0.22	1.12
C4		0.15	20	0.22	0.62

Table 1

Calibration parameters and mass accuracy of the three tested configurations.

is easier to set up for the experiments due to limits of the field of view of the camera, is not significantly different from calibrating with a larger mass range.

The five calibration and fitted curves for the repeatability tests are shown in Figure 6. Linear fits in panel Fig. 6 were done for each calibration curve independently and the average RMSE is 5.26 mg. Panel Fig. 6 shows the results from the leave-one-out cross-validation. The average slope value from the 5 combinations was \pm std. dev. was 6.150 ± 0.004 g/mm and the average RMSE error was 9.17 mg, about 1.75 times larger than the individual fits.

The developed prototype and the calibration curves demonstrate the possibility to measure water mass changes in individual vials non-destructive and non-invasively by using mechanical deflection and optical sensing. The proposed strategy leverages the previously proposed strategy based on a wire-sensing system [12] that suffered from hysteresis and excessive oscillations due to the high compliance of the springs. Additionally, tiny slips of the contact points of the balls and baskets would affect repeatability. Hysteresis still needs to be evaluated in our proposal, however robustness to oscillations already provides a potential improvement on throughput and calibration time since the beam settles down after 5-10 seconds from a perturbation.

We define the precision of the measurement σ_m as the mass prediction error when the centroid value is varied by 3 standard deviations. The baseline configuration with $D = 0.6$ m achieved a RMSE of 5.81 mg with $\sigma_m = 2.45$ mg over a 3 g range with a <30 minutes calibration routine, which also improves the wire-sensing system [12] at the single vial level. However, only one beam was fabricated and calibrated in this work, thus multiple beam sensors must

Mass Measurement of Vials during Lyophilization

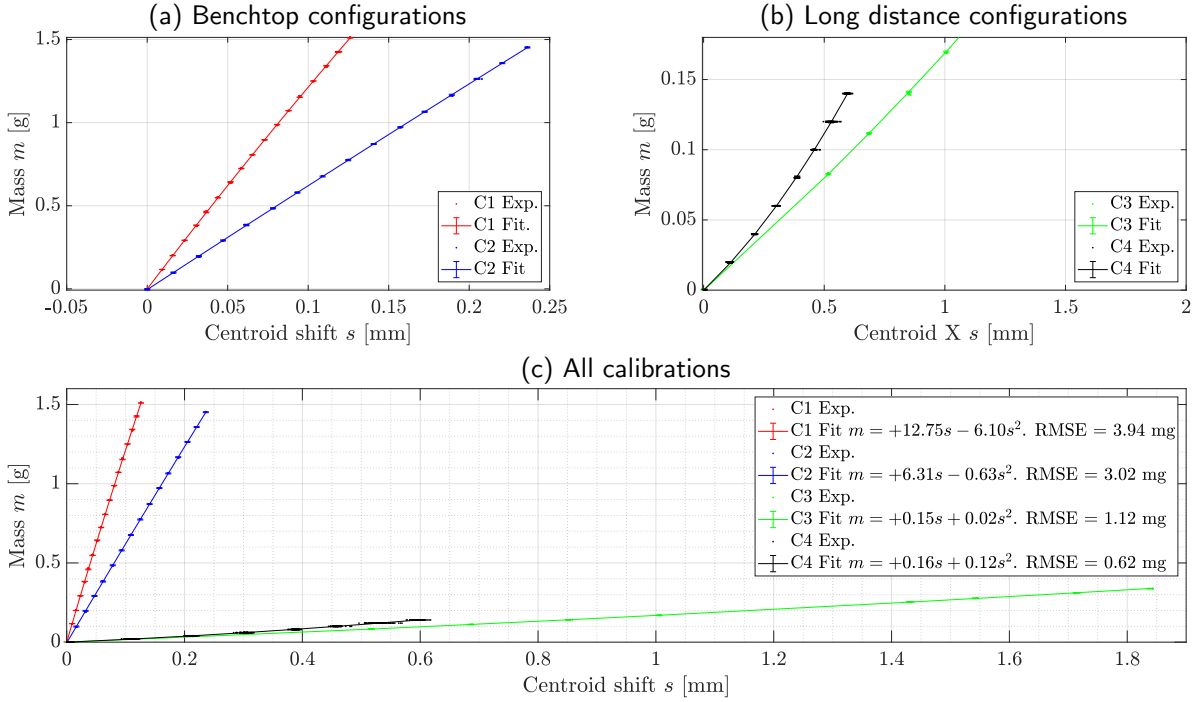


Figure 4: Calibration curves for the three configurations (top row) and overlaid in the same plot (bottom row) for ease of comparison.

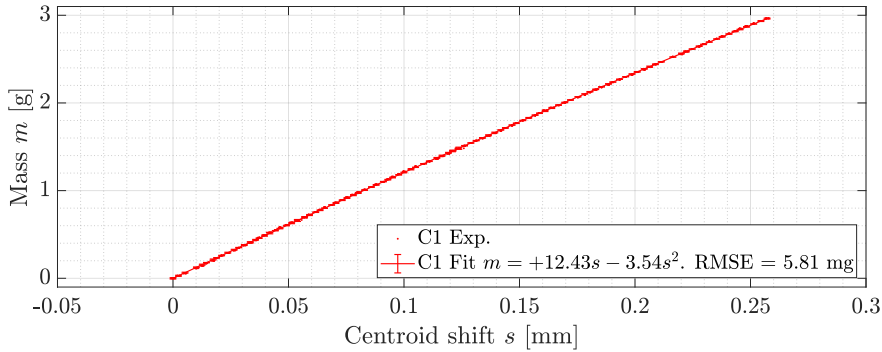


Figure 5: Calibration curve for configuration C1 for the full mass range 3 g.

be calibrated in the future to determine the inter- and intra-sensor variability. Proof-of-concepts configurations C2 and C3 demonstrated the possibility to further push the mass change sensitivity to achieve the target of 1 mg. While configuration C3 reached an RMSE of 1.12 mg with $\sigma_m = 0.37$ mg, close to the target, this result is not entirely reliable due to the observed high variability of the ground-truth mass measurements from the balance, which was improved by using the pipette method in C4, achieving a sub-mg accuracy.

In all tests with prototype I, a second-order fit was necessary to achieve a proper RMSE, which can be explained by the non-linearity of Eq. (3), non-linearities of the optical lever that are disregarded by the small angle approximation, and potential non-linear mapping of the camera due to the relatively short working distance, not considered in the model. For prototype II, the laser was aligned to make sure the center field-of-view of the camera was used, with the goal of reducing the impact of field distortions. Interestingly, the calibration curves with prototype II only required first-order fitting, suggesting the nonlinearities in the first tests arose from the camera's field distortions.

Manufacturing of the cantilever beam is foreseen to be straightforward and scalable due to the small number of parts and assembly steps required, using methods such as water-jet cutting and adhesive bonding to create the vial

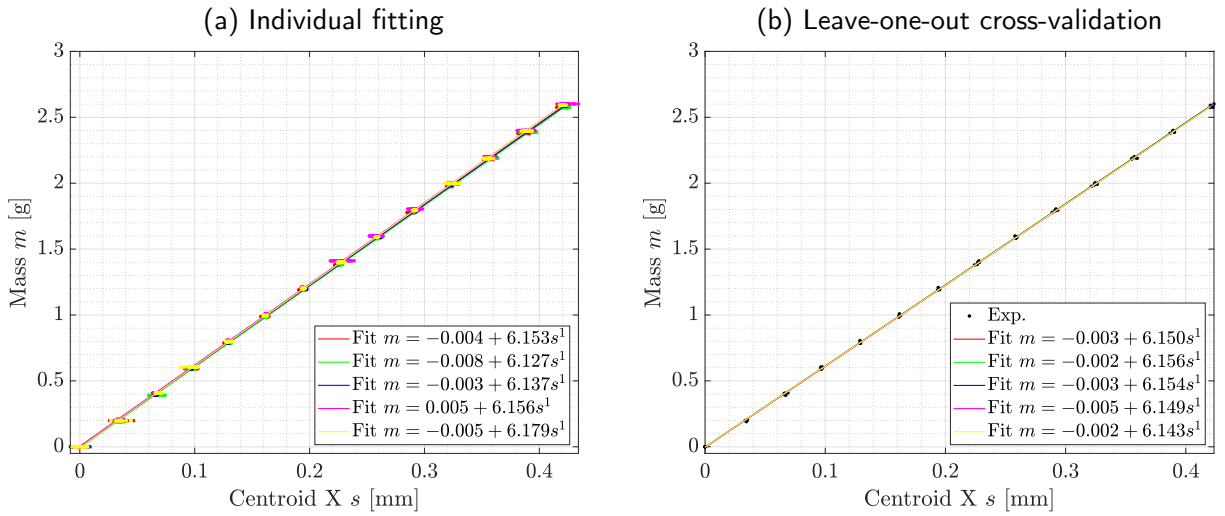


Figure 6: Prototype to evaluate and calibrate the mass sensing system, in configuration C3 (i.e., with the camera and screen separated from the main frame, and the steering mirror at 45 deg).

and mirror assembly. While individual calibration is undesirable, global calibration is challenged by the manufacturing tolerances in beam thickness and position of the vial, since both t and l are parameters that greatly affect the beam deflection. The kinematic coupling designed to hold the vial proved to help in achieving reproducible calibration curves, with similar slopes values and small average RMSE.

On the other hand, the optical sensing system can be cumbersome to integrate with the lyophilizer, specially if a very long distance is necessary to achieve the desired mass resolution. Suitable opto-mechanical integration would facilitate the laser and camera alignment, and strategies to shorten the footprint while increasing the optical path length for high deflection sensitivity can be achieved with mirrors such as in an etalon configuration. In this work we utilized a single laser-camera pair, however multiple lasers-cameras can be integrated to increase throughput and robustness to oscillations.

Material selections for the developed prototype were made for a bench-top setup and to determine the validity of this proof-of-concept device. Future integration in a lyophilization machine would require a re-evaluation of material selection while preserving the relevant material properties. For example, the 304 stainless steel beam can be replaced with 17-4PH stainless steel for vacuum compatibility and low creep at cryogenic temperatures, while preserving the mechanical deflection properties. Moreover, the double-sided tape used to integrate the cantilever beam with the support, the vial and the mirror can be replaced with vacuum-rated, low-outgassing adhesives.

5. Conclusions and Further Work

This work presents a novel, non-invasive system for inline mass measurement of individual vials during lyophilization using a cantilever beam and optical lever configuration. By translating small mass changes into amplified optical displacements, the system demonstrated sub-milligram sensitivity (down to 0.62 mg RMSE) in a prototype setup. The design preserves sterility, avoids electrical passthroughs, and is compatible with existing continuous lyophilization platforms. Intra-sensor repeatability test demonstrate consistent calibration curves for 5 independent runs. Compared to existing batch-level or post-process methods, this approach offers the potential for improved process control, reduced cycle times, and increased throughput.

Integrated into commercial drug manufacturing, our device has the potential to improve throughput and reliability in extending shelf life of drugs by providing more control over the manufacturing process.

Future work will focus on validating the system in a real lyophilization environment, addressing integration challenges such as optical alignment, environmental stability, and footprint constraints. The lowest (0.62 mg) RMSE was found on a 14 m optical path length setup. However, sub-milligram accuracy is theoretically possible on a 4 m setup. Precision manufacturing methods and high-grade calibration scales would improve accuracy and repeatability. Additionally, implementing magnetic damping can reduce vibration-induced noise, and optical cavities may be

employed to minimize the system footprint while maintaining sensitivity. Full-system calibration and performance testing under lyophilization conditions will be essential to demonstrate readiness for industrial deployment.

A. Calibration Comments

A.1. Theoretical Accuracy Estimates

The expected mass resolution for each optical configuration was estimated using the centroid uncertainty of the camera and the geometric amplification from the optical lever. Assuming a constant centroid resolution of $\delta_{\text{res}} = 0.26 \mu\text{m}$ (measured for configuration C1 under static conditions), the theoretical minimum detectable mass changes were calculated using Eq. (1). The resulting lower-bound mass resolutions were 5.1 mg (C1), 2.4 mg (C2), and 0.22 mg (C3). These estimates assume ideal optical alignment and no additional vibration or noise sources, and serve as performance limits.

A.2. Calibration Procedure

To determine actual system accuracy, the cantilever beam with attached vial was placed on an analytical balance (accuracy: 0.1 mg), which provided real-time mass readings via serial communication. Incremental water mass was added using a programmable syringe pump built with a 12.5 mm inner-diameter plunger, while the corresponding laser spot displacement was recorded by the optical system. Calibration was primarily performed with configuration C1 in static conditions, with results extrapolated to other configurations.

B. Governing Physics

B.1. Cantilever Beam Equations

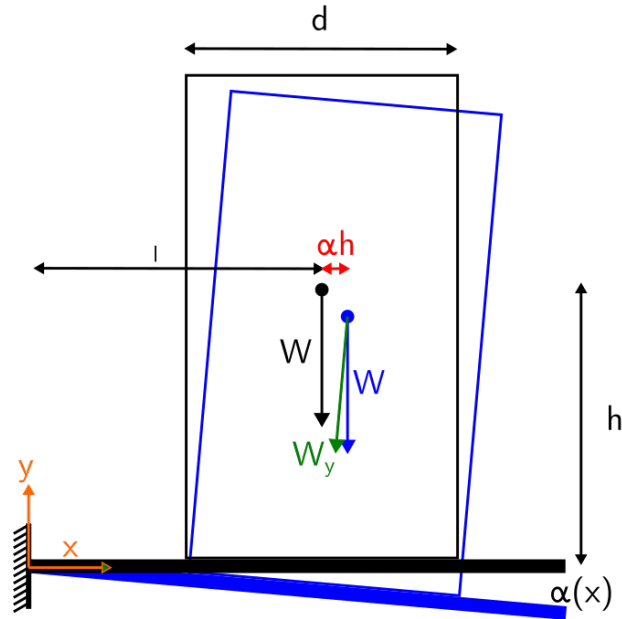


Figure 7: Free-body diagram of tilting object on a bending cantilever beam.

To model the beam deflection, we can start with the cantilever equation

$$EI \frac{d^2 y}{dx^2} = M(x),$$

where E is Young's modulus, I is second-moment of inertia, $M(x)$ is moment at horizontal coordinate x going from $x = 0$ at the fixed end of the beam and $x = L$ at the free end, and y is the vertical coordinate. For an object with center

of mass (CM) at height h from the beam, the instantaneous horizontal location x_{CM} varies as $x_{\text{CM}} = l + \alpha h$ under small angle approximation, where $\alpha = \frac{dy}{dx}$ is the beam's slope and l is the initial horizontal distance when $\alpha = 0$. The distance from the point load to a point of interest x along the beam is $l + \alpha h - x$, thus

$$EI \frac{d^2y}{dx^2} = W \left(l + \frac{dy}{dx} h - x \right)$$

$$EI \frac{d^2y}{dx^2} = Wh \frac{dy}{dx} - Wx + Wl$$

$$\frac{d^2y}{dx^2} = \frac{Wh}{EI} \frac{dy}{dx} - \frac{W}{EI} x + \frac{Wl}{EI}.$$

Note that the usual cantilever equation is recovered for $h = 0$ as expected. Also note that we should use the y -component of W in place of W , but under the small angle approximation $W_y \approx W$ which greatly simplifies equation. The differential equation can be written as

$$\frac{d\alpha}{dx} = A\alpha + Bx + C,$$

where the solution is

$$\alpha(x) = -\frac{B}{A^2}(1 + Ax) - \frac{C}{A} + D \exp(Ax). \quad (5)$$

With the boundary condition $\alpha(0) = 0$ we find $D = \frac{1}{A^2}(B + CA)$. Substituting A , B , C and D we get

$$\alpha(x) = \frac{x-l}{h} + \frac{EI}{Wh^2} - \left(\frac{EI - Whl}{Wh^2} \right) \exp\left(\frac{Wh}{EI}x\right). \quad (6)$$

The object will topple if the instantaneous horizontal position of the center of mass $h\alpha$ falls outside the base. If the object base length is d , then the stability criterion is $h\alpha < \frac{d}{2} \cos \alpha$. The design of the cantilever beam should satisfy the stability criterion to prevent the vials from toppling.

Since $Ax = \frac{Wh}{EI}x \approx 0$, we can approximate the exponential in Eq. (6) using $\exp(x) = 1 + x + \frac{x^2}{2}$, resulting in

$$\alpha(x) = -\frac{Wx^2}{2EI} \left(1 - \frac{Wl}{EI}h \right) + \frac{Wlx}{EI}. \quad (7)$$

Integrating $\alpha(x) = \frac{dy}{dx}$ we can find the deflection $y(x)$ as

$$y(x) = -\frac{Wx^3}{6EI} \left(1 - \frac{Wl}{EI}h \right) + \frac{Wlx^2}{2EI}. \quad (8)$$

Note that with $h = 0$ we recover the usual deflecting beam equation (i.e., no vertical offset in the center of mass).

The maximum angle α_{max} occurs at $x = l + \alpha h$, i.e. at the position of the center of mass. However, plugging it in Eq. (7) makes it difficult to solve for α . Instead, we can assume the maximum angle occurs at $x = l$ since $l \gg \alpha h$, which results in

$$\alpha_{\text{max}} = \frac{Wl^2}{2EI} \left(\frac{Wl}{EI}h + 1 \right) \quad (9)$$

$$y_{\text{max}} = \frac{Wl^3}{6EI} \left(\frac{Wl}{EI}h + 2 \right). \quad (10)$$

which again converges to the simple beam equation with $h = 0$.

B.2. Optical Lever

Consider the optical lever shown in Figure 8. Assume two situations. In situation 1, the cantilever beam is flat, $\alpha = 0$, and the laser is incident at an angle θ with respect to the cantilever beam's normal. According to the *law of reflection*, the reflected angle with respect to the normal is also θ . In situation 2, the cantilever beam is at an small angle $\alpha \neq 0$. The incident angle between the laser and the cantilever beam's normal is therefore $\theta - \alpha$ and using the law of reflection the reflected angle is also $\theta - \alpha$. Comparing the two situations, we conclude that the angle between the two reflected laser beam is 2α .

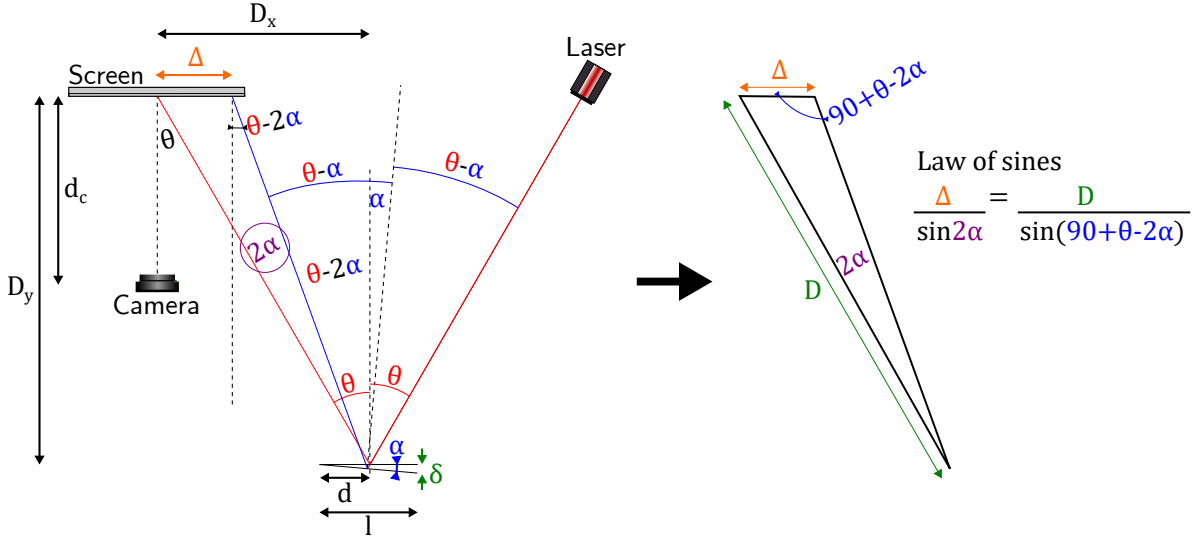


Figure 8: Schematic of an optical lever to amplify small deflections.

Using the law of sines, we can write

$$\frac{\Delta}{\sin 2\alpha} = \frac{D}{\sin(\pi/4 + \theta - 2\alpha)},$$

where Δ is the shift between the two laser spots at the screen plane and D is the distance from the cantilever beam to the center of the viewing plane. Using small angle approximation, $\sin 2\alpha \approx 2\alpha$ and $\sin(\pi/4 + \theta - 2\alpha) = \cos(\theta - 2\alpha) \approx \cos(\theta)$, yielding

$$\begin{aligned} \frac{\Delta}{2\alpha} &= \frac{D}{\cos(\theta)} \\ \alpha &= \frac{\Delta}{D} \frac{2}{\cos \theta}. \end{aligned} \quad (11)$$

Note that the factor 2 arises from the law of reflection whereas the factor of $\cos \theta$ arises from the fact that the screen is parallel to the cantilever beam, not the the incident laser. A shift Δ at the screen plane is magnified at the sensor to a shift $s = m_C \Delta$, where $m_C = \frac{f}{f - d_c}$ is the camera magnification with focal length f at a working distance d_c . Note that $m_C \in [-1, 0)$, indicating the image is inverted and de-magnified. Combining this with Eq. (11) we obtain

$$\alpha = \frac{s}{D} \frac{2}{m_C \cos \theta}. \quad (12)$$

B.3. Combining Cantilever Beam and Optical Level model

If we set δ_{res} to be the resolution of the camera to sense a shift of the laser spot, and $m_{\text{res}} = 1 \text{ mg}$ as our target minimum change in mass, then $W_{\text{res}} = 9.81 \text{ } \mu\text{N}$ and we can use Eqs. (9) and (12) to calculate the thickness of the

cantilever beam t that maps 1 mg change in mass into a shift δ_{res} at the detector plane,

$$\frac{Wl^2}{2EI} \left(\frac{Wl}{EI} h + 1 \right) = \frac{\delta_{\text{res}}}{D} \frac{2}{m_C \cos \theta}$$

where $I = \frac{wt^3}{12}$ is the second moment of a rectangular cross-section with width w and thickness t . Solving for I first and then for t we find

$$I = \frac{l^2 W D m_C \cos \theta}{8 \delta_{\text{res}} E} \left(1 + \sqrt{1 + \frac{16 \delta_{\text{res}} h}{l D m_C \cos \theta}} \right)$$

$$\frac{wt^3}{12} = \frac{l^2 W D m_C \cos \theta}{8 \delta_{\text{res}} E} \left(1 + \sqrt{1 + \frac{16 \delta_{\text{res}} h}{l D m_C \cos \theta}} \right)$$

$$t = \left[\frac{3l^2 W D m_C \cos \theta}{2 \delta_{\text{res}} E w} \left(1 + \sqrt{1 + \frac{16 \delta_{\text{res}} h}{l D m_C \cos \theta}} \right) \right]^{1/3}.$$

In practice, actually fix the beam's thickness and instead solve for the beam-to-sensor distance D which is a parameter that is relatively easy to adjust in the setup,

$$D = \frac{4 \delta_{\text{res}} E^2 I^2}{l^2 W m_C \cos \theta (l h W + E I)}. \quad (13)$$

Finally, we can solve for the instantaneous mass $m = \frac{W}{g}$ or the instantaneous laser spot displacement s

$$m(s) = \frac{EI}{2glh} \left(\sqrt{1 + \frac{16h}{l D m_C \cos \theta}} - 1 \right) \quad (14)$$

$$s(m) = m \frac{gl^2 D m_C \cos \theta}{4E^2 I^2} (m l h g + E I) \quad (15)$$

B.4. Example

For a setup with the parameters shown in Figure 9, a distance of $D = 2.38$ m maps a 0.26 mg mass change to a laser spot shift of $\delta = 1 \mu\text{m}$. Figure 10 is a plot of Eq. (15) for the same example, showing a nearly linear relationship between s and m , which can be analytically obtained by using the approximation $l h m g \ll 2 E I$.

B.5. Magnetic Damping Aside

Magnetic damping was considered as a means to suppress cantilever oscillations induced by motion of the planar motors as the vials moved throughout the system. The otherwise small effects of vibration are amplified by the optical lever and thus negatively affect laser spot detection accuracy. The damping approach involved placing magnets beneath the conductive beam to generate eddy currents that oppose motion and dissipate energy. This creates a nonlinear damping term that scales approximately with the inverse seventh power of the beam's height above the magnets. Although analytically viable, the strategy was ultimately deemed unnecessary due to the beam's high stiffness in the direction of motor-induced excitation. As a result, no measurable improvement in damping performance was observed in practice.

Mass Measurement of Vials during Lyophilization

Cantilever beam	Inputs	Thickness	t	0.2032	mm	Beam geometric input
		Width	w	10	mm	Beam geometric input
		Height of vial's center of mas	h_cm	22.5	mm	Beam geometric input
		Beam length	L	35	mm	Beam geometric input
		Load position (from fixed end)	a_0	35	mm	Beam geometric input
		Laser position (from fixed end)	a_l	35	mm	Beam geometric input, must be > a_0
		Min mass change	dm_min	1	mg	Sensing parameter input
		Mass sensing range	dm_max	3	g	Sensing parameter input
		Max mass	m_max	25	g	Sensing parameter input
	Intermedate calculations	Young's Modulus	E	193	GPa	Beam material property input
		Density	ρ	7930	kg/m ³	Beam material property input
		Second moment of area	I	6.99E-03	mm ⁴	
		Beam weight	W_b	0.16	N/m	
	Outputs	Min force change	dW_min	0.0000981	N	
		Force sensing range	dW_max	0.0294	N	
		Max force change	W_max	0.245	N	
		Min deflection	dy_min	103.9	nm	Beam output, deflection using mass change resolution
		Sensing deflection range	dy_max	313.0	μm	Beam output, deflection using mass change range
Max deflection		y_max	2.7	mm	Beam output, deflection using entire mass	
Self-weight deflection		y_self	22.0	μm	Beam output, self deflection using only beam mass	
Max stress		σ_max	125	MPa	Beam output, stress using entire mass, must be < Yield strength	
Optical lever		Input	Centroid resolution	delta	0.26	μm
	Laser incident angle		theta	10	degrees	Optical lever input
	Camera focal length		f	6.65	mm	Optical lever input
	Camera working distance		d_WD	140	mm	Optical lever input
	Camera magnification		m	-0.05	Dimensionless	Optical lever output, camera magnification
	Calculation	Beam to sensor distance	D	2.38	m	Optical lever output
		Sensing spot displacement range	L_s	16	mm	Optical lever output, displacement using mass change range
		Initial spot displacement	L_s0	135	mm	Optical lever output, displacement using entire mass

Figure 9: Example spreadsheet for a cantilever beam and optical lever design.

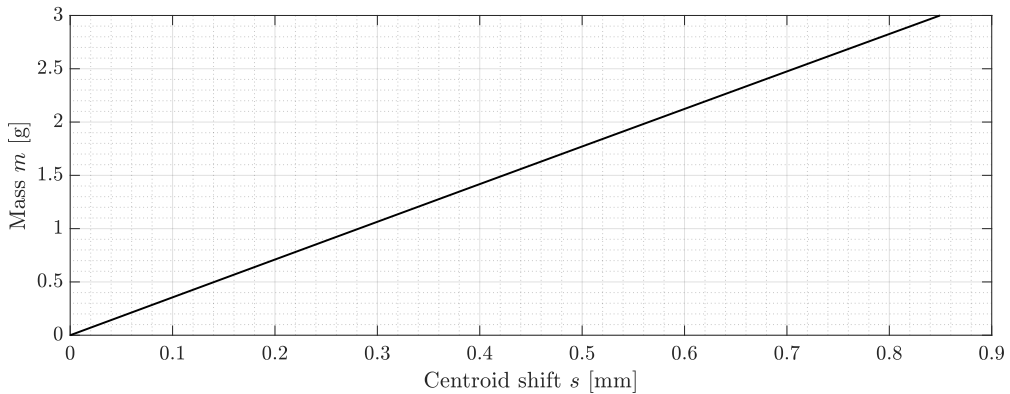


Figure 10: Simulated mass to laser spot displacement for the cantilever beam and optical lever system.

C. Capacitance strategy details

We first analyzed a classical parallel-plate geometry in which two 1 cm² copper electrodes are situated on opposite sides of the standard 24 mm vial. The plates are then separated by $d = 24$ mm, and the standard relation $C = \frac{\epsilon_0 \epsilon_r A}{d}$ predicts a dry matrix capacitance of about 149 fF. Introducing the pharmaceutical limit of 1% residual moisture content [15] would cause an increase in capacitance of approximately 28 fF. Although even attofarad resolution bridges are available [16], most easily accessible capacitance meters only resolve 50 fF reliably, rendering this arrangement impractical for routine process monitoring.

To amplify the signal, we then examined interdigitated coplanar electrode arrangements in which the electrodes reside on a single surface of the vial, for example directly underneath the vial (Figure 11). Following the conformal-mapping treatment of coplanar strips reported by [17, 18], the capacitance of a single coplanar electrode pair shown in Figure 11 is

$$C = \epsilon_0 \epsilon_{\text{eff}} L \frac{K(k')}{K(k)},$$

where L is the overlap length of the fingers, $K(\cdot)$ denotes the complete elliptic integral of the first kind, and the modulus and complementary modulus are

$$k = \frac{d}{2s + d}, \quad k' = \sqrt{1 - k^2}.$$

The effective permittivity ϵ_{eff} reflects the two dielectric layers that separate the electrodes from free space: the glass vial wall (height h_w , relative permittivity ϵ_w) and the lyophilized product (height h_p , relative permittivity ϵ_p):

$$\epsilon_{\text{eff}} = 1 + \frac{K(k)}{2K(k')} \left[\frac{K(k'_p)}{K(k_p)} (\epsilon_p - 1) + \frac{K(k'_w)}{K(k_w)} (\epsilon_w - \epsilon_p) \right],$$

with

$$k_i = \frac{\tanh\left(\frac{\pi d}{4h_i}\right)}{\tanh\left(\frac{\pi(2s+d)}{4h_i}\right)}, \quad k'_i = \sqrt{1 - k_i^2}, \quad i \in \{p, w\}.$$

Numerical example. For a representative finger width $s = 500 \mu\text{m}$, gap $d = 100 \mu\text{m}$, finger length $L = 1 \text{ cm}$, glass wall thickness $h_w = 1 \text{ mm}$ and $\epsilon_w = 4$ (borosilicate), together with a fully dried matrix of relative permittivity $\epsilon_p = 3.3$ we have:

$$C_{\text{dry}} \approx 1.16523 \text{ pF}.$$

An interdigitated array comprising 100 identical finger pairs therefore exhibits an effective capacitance of $C_{\text{dry,total}} = 100C_{\text{dry}} \approx 116.523 \text{ pF}$. If the residual-moisture content in the lyophilized matrix rises to the pharmaceutical limit of 1% [15], the relative permittivity of the product can be approximated by a linear mixture,

$$\epsilon'_p = 0.99 \epsilon_p + 0.01 \epsilon_{\text{water}} = 4.051,$$

and the electrode-pair capacitance becomes $C_{\text{wet}} \approx 1.16904 \text{ pF}$. The corresponding incremental change

$$\Delta C = C_{\text{wet,total}} - C_{\text{dry,total}} \approx 381 \text{ fF}$$

which lies comfortably within the 50 fF resolution of commodity capacitance meters, confirming the practicality of the approach. In practice, the moisture profile within the vial is not uniform because sublimation proceeds from the exposed top surface downward. The bottom surface of the vial will therefore retain a higher water fraction, leading to an even larger base capacitance during drying.

References

- [1] J. Barley, Basic Principles Of Freeze-Drying, 2022. URL: <https://scientificproducts.com/white-papers-tech-notes/basic-principles-of-freeze-drying/>.
- [2] D. Awotwe-Otoo, M. A. Khan, Lyophilization of Biologics: An FDA Perspective, in: D. Varshney, M. Singh (Eds.), Lyophilized Biologics and Vaccines, Springer New York, ????, pp. 341–359. URL: https://link.springer.com/10.1007/978-1-4939-2383-0_15. doi:10.1007/978-1-4939-2383-0_15.
- [3] T. McCoy, R. Affleck, D. Khamar, Considering Residual Moisture Measurement in Lyophilized Drug Product, American Pharmaceutical Review (2019). Publisher: Sanofi SA.
- [4] E. Joseph, Residual Moisture Determination in Lyophilized Drug Products, Pharmaceutical Technology 43 (2019) 30–39, 56. Publisher: MJH Life Sciences.

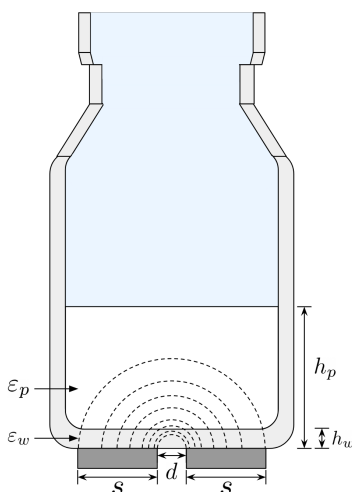


Figure 11: An illustration of the capacitance-based residual moisture measurement strategy with a single pair of coplanar electrodes separated by a distance d .

- [5] S. Ohtake, S. Feng, E. Shalaev, Effect of Water on the Chemical Stability of Amorphous Pharmaceuticals: 2. Deamidation of Peptides and Proteins, *Journal of Pharmaceutical Sciences* 107 (2018) 42–56.
- [6] S. Rambhatla, S. Tchessalov, M. J. Pikal, Heat and mass transfer scale-up issues during freeze-drying, III: Control and characterization of dryer differences via operational qualification tests 7 (???) E61–E70.
- [7] R. Pisano, Automatic control of a freeze-drying process: Detection of the end point of primary drying, *Drying Technology* 40 (2022) 140–157. Publisher: Taylor & Francis _eprint: <https://doi.org/10.1080/07373937.2020.1774891>.
- [8] D. Fissore, R. Pisano, A. A. Barresi, On the Methods Based on the Pressure Rise Test for Monitoring a Freeze-Drying Process, *Drying Technology* 29 (2010) 73–90. Publisher: Taylor & Francis _eprint: <https://doi.org/10.1080/07373937.2010.482715>.
- [9] W. J. Kessler, E. Gong, Tunable Diode Laser Absorption Spectroscopy in Lyophilization, in: K. R. Ward, P. Matejtschuk (Eds.), *Lyophilization of Pharmaceuticals and Biologicals: New Technologies and Approaches*, Springer, New York, NY, 2019, pp. 113–141. URL: https://doi.org/10.1007/978-1-4939-8928-7_5. doi:10.1007/978-1-4939-8928-7_5.
- [10] A. Massei, N. Falco, D. Fissore, NIR-Based Real-Time Monitoring of Freeze-Drying Processes: Application to Fault and Endpoint Detection, *Processes* 13 (2025) 452.
- [11] T. R. M. De Beer, P. Vercruyse, A. Burggraave, T. Quinten, J. Ouyang, X. Zhang, C. Vervaet, J. P. Remon, W. R. G. Baeyens, In-line and real-time process monitoring of a freeze drying process using Raman and NIR spectroscopy as complementary process analytical technology (PAT) tools, *Journal of Pharmaceutical Sciences* 98 (2009) 3430–3446.
- [12] S. J. Burcat, R. P. Kadambi, L. Stratta, R. D. Braatz, R. Pisano, B. L. Trout, A. H. Slocum, Vacuum Compatible SpringWire System for Mass Measurement of Vials during Lyophilization, 2025. Publisher: Massachusetts Institute of Technology and Politecnico di Torino.
- [13] S. Alexander, L. Hellemans, O. Marti, J. Schneir, V. Elings, P. K. Hansma, M. Longmire, J. Gurley, An atomic-resolution atomic-force microscope implemented using an optical lever, *Journal of Applied Physics* 65 (1989) 164–167.
- [14] KAB Electro Acoustics, Dielectric constant chart: Dielectric constants of common materials, <https://www.kabusa.com/Dielectric-Constants.pdf>, n.d. Accessed 11 May 2025.
- [15] Center for Biologics Evaluation and Research, Guideline for the Determination of Residual Moisture in Dried Biological Products, Technical Report Docket No. 89D-0140, Food and Drug Administration, Bethesda, MD, 1990. URL: <https://downloads.regulations.gov/FDA-2015-D-3399-0011/content.pdf>, prepared by the Division of Biochemistry and Biophysics, Laboratory of Analytical Chemistry (HFB-740).
- [16] J. Chen, B. McGaughy, D. Sylvester, C. Hu, An on-chip, attofarad interconnect charge-based capacitance measurement (cbcm) technique, in: *International Electron Devices Meeting. Technical Digest*, 1996, pp. 69–72. doi:10.1109/IEDM.1996.553124.
- [17] S. Gevorgian, H. Berg, Line capacitance and impedance of coplanar-strip waveguides on substrates with multiple dielectric layers, in: *2001 31st European Microwave Conference*, 2001, pp. 1–4. doi:10.1109/EUMA.2001.339161.
- [18] A. A. Nassr, W. H. Ahmed, W. W. El-Dakhkhni, Coplanar capacitance sensors for detecting water intrusion in composite structures, *Meas. Sci. Technol.* 19 (2008) 075702.